Journal of Hydrology 612 (2022) 128217

Contents lists available at ScienceDirect

Journal of Hydrology

journal homepage: www.elsevier.com/locate/jhydrol

Research papers

Unpiloted Aerial Vehicle (UAV) image velocimetry for validation of two-dimensional hydraulic model simulations

Christopher Masafu [a,*], Richard Williams [b], Xiaogang Shi [a,*], Qiangqiang Yuan [c], Mark Trigg [d]

[a] School of Interdisciplinary Studies, University of Glasgow, Dumfries DG1 4ZL, UK
[b] School of Geographical and Earth Sciences, University of Glasgow, Glasgow G12 8QQ, UK
[c] School of Geodesy and Geomatics and the Collaborative Innovation Center for Geospatial Information Technology, Wuhan University, China
[d] School of Civil Engineering, University of Leeds, Leeds LS2 9JT, UK

ARTICLE INFO

This manuscript was handled by J. Simunek, Editor-in-Chief, with the assistance of Zaher Mundher Yaseen, Associate Editor

Keywords:
Unpiloted Aerial Vehicle (UAV)
Image velocimetry
Surface velocity
LSPIV
Model validation
Probability concept

ABSTRACT

Non-intrusive image-based techniques for measuring surface river velocities have rapidly evolved as a cost-effective and safe means for quantifying flow patterns. Large-scale particle image velocimetry (LSPIV) can provide instantaneous surface velocities over a large spatial footprint rapidly and with little pre-calibration as compared to traditional techniques. Assessment of the spatial distribution of flow velocities in hydraulic models has been comparatively harder to achieve than assessment of depth due to logistical challenges but would be aided using large observational datasets that represent the variability and distribution of flow hydraulics. Additionally, the efficacy of image velocimetry in assessing the accuracy of outputs from 2D hydraulic models has not been addressed. Here, we demonstrate how LSPIV can be used to calibrate and validate 2D model predictions in a gravel bed river reach. LSPIV velocities are depth-averaged using standard velocity coefficients (α) and then using the Probability Concept (PC) - a probabilistic formulation of velocity distributions that accounts for non-standard velocity profiles, typical in field settings. UAV surveys were used to acquire video for LSPIV and imagery for Structure from Motion (SfM) topographic modelling. We use spatially dense acoustic doppler current profiler (aDcp) velocity data for benchmark assessment of the velocity outputs of HEC-RAS 2D model simulations. 2D model prediction error, based on seeded LSPIV velocities, was within range (4.2%) of the aDcp parametrised model, with improvements in modelled versus predicted velocity correlations (up to 7.7%) when using PC to depth average LSPIV velocities. Validation bias reduced significantly (11%) with tighter error distributions when compared to the aDcp based model. Although additional hydraulic measurements are required to parametrise the Probability Concept algorithm, the performance of 2D hydraulic models calibrated/validated with LSPIV velocities is on par with traditional techniques, demonstrating the potential of this non-intrusive, low-cost approach.

1. Introduction

Two-dimensional (2D) hydraulic modelling has been widely used to assess flood risk at varying temporal (such as hourly to daily) and spatial scales (including regional to catchment). The assessment of 2D model simulations has previously been achieved by comparing model outputs to observations of water surface elevations, extents, and depths (Bernhofen et al., 2018; Cea et al., 2014) and, less commonly, velocity (Barker et al., 2018; Fischer et al., 2015). Previous investigations (e.g., Gard, 2008; Lane et al., 1999; Pasternack et al., 2006; Williams et al., 2013) utilized velocity measurements collected using conventional sensors (acoustic Doppler current profilers; aDcp) to assess 2D model performance. However, the use of velocity observations obtained using traditional measurements to assess 2D models has notable challenges, including safety considerations during high discharge events and limitations on the spatial extent of observations that can be acquired. There remains a pressing need for velocity data that fully samples the range and distribution of channel velocities to validate 2D hydraulic models (Barker et al., 2018; Cea et al., 2014; Wagner and Mueller, 2001).

The advent of powerful, cost-efficient computing power and precise remote sensing datasets has offered an avenue for new, high quality, fine spatial scales benchmark data, for the validation of flood models (Wing et al., 2017). In particular, the use of Unpiloted Aerial Vehicles (UAVs) as a non-contact method to investigate flood extents has eliminated the

* Corresponding authors at: School of Interdisciplinary Studies, University of Glasgow, Dumfries DG1 4ZL, UK
E-mail addresses: masafu@gmail.com (C. Masafu), John.Shi@glasgow.ac.uk (X. Shi).

https://doi.org/10.1016/j.jhydrol.2022.128217
Received 27 January 2022; Received in revised form 26 May 2022; Accepted 11 July 2022
Available online 19 July 2022

need to deploy staff in dangerous field conditions (DeBell et al., 2016; Eltner et al., 2020; McCabe et al., 2017; Perks et al., 2020; Tokarczyk et al., 2015). The fine spatial and temporal resolution of UAV data has also allowed for the mapping of velocity dynamics of flood events at unprecedented scales (Al-mamari et al., 2019; Smith et al., 2014) leading to improved insights into local catchment processes. Additionally, UAV topographic surveys based on Structure from Motion (SfM) are providing fine scale digital terrain models (DTMs), which are enhancing model parametrisation efforts, such as better descriptions of surface roughness for calibrating Mannings roughness (DeBell et al., 2016).

Image velocimetry has generated considerable interest in hydrology, presenting capabilities to derive spatially distributed surface flow velocities at high temporal resolution using UAVs as a camera platform (Koutalakis et al., 2019; Pizarro et al., 2020b; Tauro et al., 2017). Although various image velocimetry algorithms have been applied to monitor river flows (Cao et al., 2021; Perks et al., 2020), Large-Scale Particle Image Velocimetry (LSPIV) is the most commonly used algorithm and is in many respects considered proven and tested (Jodeau et al., 2017). LSPIV, the large-scale implementation of PIV techniques in outdoor environments, is based upon Eulerian principles (Euler, 2008), where the average displacement of cluster particles within an interrogation window is measured. This can be differentiated from Particle Tracking Velocimetry (PTV) methods, which are based on Lagrangian motion (Amelinckx, 1971) that tracks the motion of individual particles over time. Depth-averaged velocities may then be retrieved from LSPIV surface velocities using logarithmic velocity profiles, by fitting power laws to velocity profiles (Welber et al., 2016; Wilcock, 1996) or using a velocity coefficient to adjust surface velocities (Le Coz et al., 2010).

Whilst a great deal of research has been dedicated to the development and assessment of the performance of various image velocimetry algorithms, such as the impact of seeding densities under low flow conditions (Pearce et al., 2020), inter-comparisons of algorithm implementation under diverse hydro-geomorphic settings (Perks et al., 2020) and development of workflows to compute and benchmark surface flow velocities (Eltner et al., 2019), few studies have systematically assessed the accuracy of LSPIV based surface flow velocities in natural environments. The need for high quality data to validate flood models, coupled with a benchmark evaluation of image velocimetry data in both high and low flows, has significant potential in reducing uncertainty associated with spatially distributed model predictions.

Research evaluating the capability of 2D hydraulic models to accurately reproduce the spatial distribution of water velocity has been limited. Several studies have validated 2D models using aDcp velocity data. For example, Williams et al. (2013) demonstrated the capability of spatially dense RTK-GNSS (Real Time Kinematic – Global Navigation Satellite System) positioned Acoustic Doppler Current Profiler (aDcp) data in the calibration and verification of a 2D hydraulic model. Meanwhile, Barker et al. (2018) evaluated aDcp and kayak (positioned with RTK-GNSS) particle surface velocity vector methods to validate a 2D model, concluding that surface velocity tracking data outperforms fixed-point data validation for all the statistical validation metrics. In practice, most 2D model assessment efforts that have used velocity data have done so using limited-location samples, usually with selected cross-sections, where 1D current meter time-averaged velocity data or 2D acoustic instrumentation measurements have been collected, leaving room for significant uncertainties and errors. For example, Kasvi et al. (2015) used four aDcp cross-sections to validate a 2.1 km long 2D model, Tiffan et al. (2002) used two aDcp cross-sections to validate a 33 km long 2D model while Parsapour-Moghaddam and Rennie (2018) used one aDcp cross-section to validate a 0.19 km long 3D model. They all concluded that more field data would have resulted in more robust validation outcomes. When simulating flow dynamics using 2D models, a small number of cross-sections to assess model simulations are insufficient. It is also time-intensive to identify appropriate cross-sections and then gather velocity measurements. Further, classical wading and aDcp methods are not evolving with the scales of model assessment required and they remain remarkably slow field techniques (Pasternack, 2011). In summary, the acquisition of aDcp velocity measurements are limited in: (i) shallow rivers, as observations can only be acquired beyond a vertical blanking distance; (ii) turbulent conditions due to boat instability and bedload transport; and (iii) high velocities due to logistical challenges. With respect to the latter challenge, in some situations remote controlled boats (Flener et al., 2015) and RTK-GNSS positioning can be used to overcome bias in bottom tracking due to bedload transport (Rennie and Church, 2010; Williams et al., 2015) but challenges monitoring high flows still remain prevalent in many situations.

Although the use of non-contact methods to estimate surface velocities in riverine environments has been demonstrated (e.g., Pearce et al., 2020; Pumo et al., 2021; Ran et al., 2016), the majority of studies have relied on a commonly established multiplicative constant known as a velocity-index, typically varying between 0.70 and 0.90, for the computation of depth-averaged velocity (Bechle and Wu, 2014). The use of a constant velocity-index for translation of surface velocities not only fails to account for atypical velocity distributions, such as when maximum velocity occurs below the water surface, but it also assumes that the vertical-velocity distributions in a river channel can be characterized using a logarithmic or power law, which is not always true (Moramarco et al., 2017). An alternative approach for accurately estimating two-dimensional velocity distributions, based on the entropy probability density function of velocity, was proposed by Chiu (1987). Previous studies have demonstrated that the maximum entropy method can be a suitable means to constrain velocity bias towards known parameters, thus serving as a suitable approach to relate surface velocities to depth-averaged velocities (Marini et al., 2011).

The first objective of this paper is to investigate whether spatially continuous surface velocities computed using LSPIV can be used to accurately calibrate and validate 2D hydraulic model simulations in a natural environment. We aim to demonstrate the utility of models fully parametrised using LSPIV, as compared to those calibrated/validated using spatially dense aDcp data. The second objective is to evaluate the utility of the entropy-based surface velocity method Chiu (1987), named Probability Concept (PC), as a mathematical basis for transforming LSPIV-derived surface velocities to depth-averaged velocities, in order to account for velocity distributions that do not conform to logarithmic or power laws within a shallow gravel-bed river. We provide an explicit assessment of the variance between numerical model velocity simulations based on aDcp observations and LSPIV derived estimates. The spatial uncertainties in 2D model simulations based on both aDcp and LSPIV are assessed using standard hydraulic model performance metrics. Advancing prior studies in this research domain (e.g., Barker et al., 2018; Pasternack et al., 2006), this work presents a hitherto untested application of spatially explicit, high-resolution LSPIV-derived velocities in calibrating and validating a 2D hydraulic model. Calibration and validation terminology used in this paper follows the definitions of Refsgaard and Henriksen (2004).

The following sections describe the study site, outline the methods that are used to generate the model topography and detail the field surveys used to acquire aDcp, LSPIV and electromagnetic flow meter measurements. The next section presents the results from 2D calibration and validation using aDcp, then LSPIV measurements. A discussion follows that examines the hydraulic predictions and assesses the uncertainty and value of both model simulations.

2. Study site

This investigation is undertaken along a restored reach of Swindale Beck, Cumbria, England (Fig. 1), which is a 13.4 km^2 sub-catchment of the River Eden. Restoration of the study reach was undertaken in 2016 and involved channel re-meandering, with 890 m of a new sinuous channel, positioned along the course of a paleochannel, replacing 750 m of straightened channel (Wildhaweswater, 2020). Post-restoration, the river is considerably more geomorphologically diverse, being

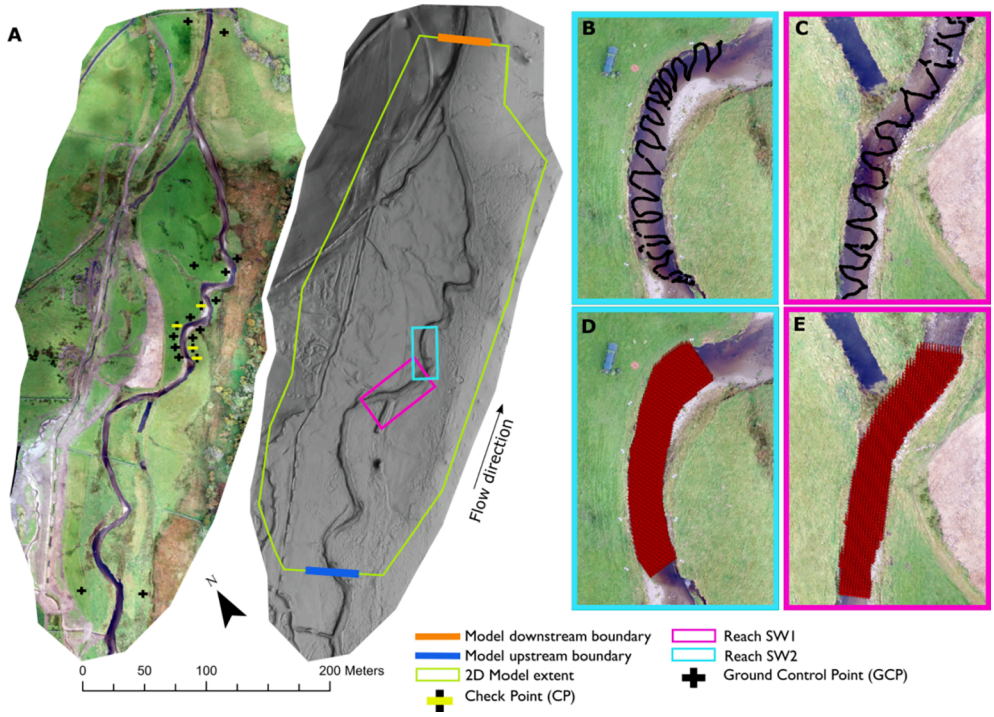

Fig. 1. (A) Orthomosaic image of the Swindale (351074E 512754 N, British National Grid) study reach (left) and hillshaded SfM DEM (right) showing the extent of the 2D model domain and investigated sub-reaches; (B, C) aDcp survey transects (black traces); (D, E) LSPIV surface velocity.

characterised by pools, riffles and gravel bars; and is geomorphologically active in response to high flow events. The floodplain is mostly vegetated with species-rich hay meadow, bog, and grassland. Catchment descriptors derived from the UK Flood Estimation Handbook (FEH) (Institute of Hydrology, 1999) were used to estimate the median annual maximum flood (QMED) which is 26.96 m^3/s. A telemetry gauging station (United Utilities station 761113) records stage in the river at a weir every 15 min from 1997 to present (Hankin et al., 2019). The extent of the 2D hydraulic model domain is shown in Fig. 1; within this extent a set of image velocimetry and aDcp observations were acquired along a reach that is approximately 540 m long.

3. Methodology

The experiments conducted within the study reach are described in the experimental framework (Fig. 2), which commenced with the acquisition of UAV imagery (still; oblique), used to generate a detailed terrain model using SfM photogrammetry (Section 3.1). UAV video sequences were subsequently acquired on 24 February 2021 over two sub-reaches (hereafter referred to as SW1 and SW2; Fig. 1).

Conventional water velocity measurements were conducted using an aDcp (Section 3.2) and a current meter (Section 3.3). aDcp river velocity measurements were collected during the falling limb of a storm event that occurred on 24 February 2021 and peaked at 20.6 m^3/s. The aDcp

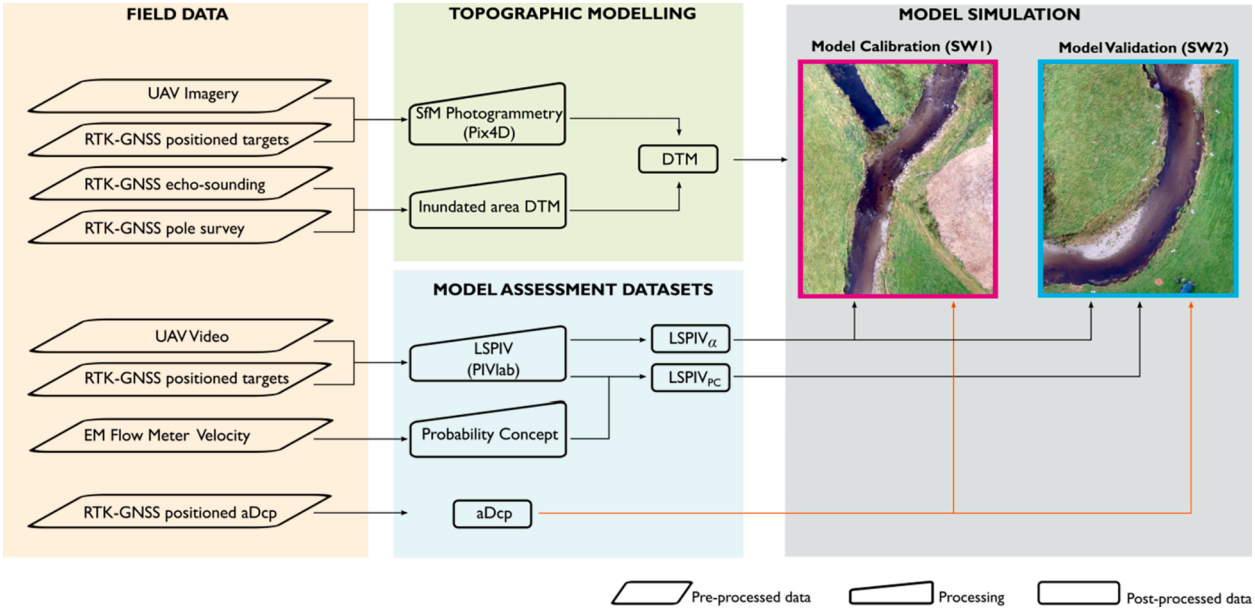

Fig. 2. Experimental framework.

dataset was processed to derive velocity magnitude vectors which were used to calibrate/validate the 2D hydraulic model. UAV videos were processed using the LSPIV algorithm, PIVlab (Thielicke and Stamhuis, 2014) to generate instantaneous surface velocity vectors (Section 3.4). A subsequent field campaign to acquire flow meter measurements was conducted on 21 June 2021 during the summer low flow period at an average discharge of 2.5 m^3/s. Flow meter measurements provided detailed vertical velocity distribution profiles that were used to parametrise the Probability Concept algorithm (Chiu, 1987) for depth averaging of LSPIV surface velocities (Section 3.5). Hydraulic modelling was then performed using a 2D model (HEC-RAS 6.0 (Brunner et al., 2020)) following which an assessment of model velocity outputs was conducted using conventional aDcp measurements and LSPIV measurements. The following sub-sections provide further details on these methods.

3.1. DTM generation

3.1.1. Inundated area: RTK-GNSS and echo-sounding

A field campaign was undertaken using a hybrid approach to map dry and inundated areas of the study reach. A Leica GS10 receiver was positioned over a surveyed base station in GNSS mode. To survey channel bathymetry within the study reach, a combination of wading surveys using a Leica GS10 antenna mounted on a pole, in RTK-GNSS mode, and vertical beam echo sounding observations from a Sontek M9 aDcp with RTK-GNSS positioning from a Leica GS16 RTK-GNSS antenna were deployed. During the wading survey, an operator traversed the river channel collecting bed, bank toe and water edge RTK-GNSS points with approximately 1 m point spacing. The resulting composite (wading-based and aDcp-based) dataset comprised over 13,000 bed level measurements with a mean density of 1.77 points m^{-2}.

A DTM of the river channel was then generated in ArcGIS Pro by interpolating a Triangular Irregular Network (TIN) from the aggregated wading and aDcp-based RTK GNSS datasets. A Delaunay conforming triangulation was used ensuring that breakline segments were densified. Linear interpolation was then used to convert the channel TIN into a 0.2 m DTM.

3.1.2. Dry areas: SfM photogrammetry

SfM with multiview stereo photogrammetry (hereafter together referred to as SfM photogrammetry (Carrivick and Smith, 2019)) was used to generate a DEM of the study area using images acquired by a DJI Phantom 4 RTK UAV. SfM photogrammetry is a technique used to generate a three-dimensional point cloud (i.e., structure) from the motion of a camera across a scene of interest (Escobar Villanueva et al., 2019). DEMs that have been generated using SfM are now widely used to investigate river floodplain environments (e.g., Annis et al., 2020; Javernick et al., 2014; Schumann and Andreadis, 2019).

Pix4D software was used for SfM photogrammetry following the method reported in Stott et al. (2020), with guidance based on James et al., (2019) (Table S1). We provide the detailed SfM processing workflow in the supplementary material (Figure S1). 944 images from the UAV were automatically geotagged with WGS84 coordinates during acquisition. These were then transformed to the ETRS89 geodetic reference system, used in the UK as the datum for the Ordnance Survey reference system. SfM processing in Pix4D was largely automated and comprised three-stages to generate both Digital Surface Models (DSMs) and bare terrain DEMs. The initial step involved the computation of key points on the images to enable matching. Matched images were then processed using automatic aerial triangulation and bundle block adjustment to create a 3D point cloud of the study area.

Manual classification of Ground Control Points (GCPs) was then carried out. A matrix of 18 ground control targets, each measuring 0.6 × 0.6 m, were laid out within the study reach on dry land. A Leica GS10 GNSS antenna, mounted on a 2 m pole, was used to observe each of the ground control targets for at least 5 min in GNSS static mode. Postprocessing of the raw GNSS observations relative to the base station observations was carried out using proprietary Leica GeoOffice software to establish the true coordinates of the ground control targets. To independently evaluate errors in subsequent processing, 5 targets were used as check points (Fig. 1a).

The second and third processing steps involved the generation of a DSM using an inverse distance weighting algorithm and generation of a bare earth DTM by classifying a dense point cloud using a proprietary Pix4D machine learning algorithm. The accuracy of the UAV-Derived DEM was acceptable (Table 1), with Root Mean Square Errors (RMSE) for CPs being < 0.05 m. The fused 0.2 m SfM DTM (Fig. 1a) served as the final topographic surface for 2D modelling.

3.2. aDcp velocity survey data

Acoustic survey velocity measurements were acquired using a SonTek M9 RiverSurveyor. The theory of aDcp system operation is discussed in detail by Kostaschuk et al. (2005) and Simpson (2001). The M9 RiverSurveyor is equipped with four profiling beams (3.0 and 1.0 MHz) and one 0.5 MHz vertical beam for depth measurement. Due to the shallow nature of the river, all velocity measurements used the 3 MHz transducers. The aDcp was mounted on an SonTek Hydroboard and calibrated as outlined by Williams et al. (2013). Accurate positioning of the moving aDcp was provided by a Leica GS16 RTK-GNSS receiver fitted on the trimaran boat. This provided RTK corrections to position depth and velocity observations.

Field aDcp surveys were conducted during a hydrograph recession in winter (February 2021). Average discharge during the survey was 13.1 m^3/s. During field measurements, the aDcp was dragged in a zig-zag trajectory by two operators standing on opposite sides of the river-bank. Each survey provided over 1000 sample points at a mean spacing of 1 m between transects (Fig. 1; B-C), with some minor spacing alterations being made to accommodate riverine features such as riffles and shallow gravel bars.

The aDcp logged approximately 1,124 georeferenced velocity ensembles in the x and y directions. Post-processing of the raw aDcp outputs focused on the horizontal components (x and y) of mean velocity. Sontek's proprietary RiverSurveyor Live software was used to export the datasets to MATLAB, where a custom script was written to extract the horizontal velocity vectors. Depth-averaged velocity magnitude was then calculated from the two horizontal velocity vectors, x and y. Measurements that failed to meet location thresholds (<4 GNSS satellite observations or where Horizontal Dilution of Precision (HDOP) was>8) were discarded (Environment Canada, 2004). Points close to the channel edges were also disregarded as the ability of aDcps in measuring shallow-water velocities is limited by side-lobe interference and the instrument's blanking distance (distance below the transducer where velocity cannot be measured) (Mueller et al., 2013).

3.3. Flow meter measurements

A Valeport Electromagnetic (EM) Flow Meter, widely used for wading measurements, was used to acquire two-dimensional water velocities (Fig. 3). The EM flow meter has an accuracy of ± 0.5 % of readings (plus 5 mm) and a range of -5 m/s to 5 m s^{-1} with the ability to operate at a minimum depth of 0.05 m. Velocity data were collected at six cross-sections. The vertical velocity profile of each vertical was sampled

Table 1
Localisation accuracy per check point and mean errors in the three coordinate directions for the SfM DTM.

Dimension	Check Points (CP)		
	X (m)	Y (m)	Z (m)
Mean Error	−0.009	−0.007	0.001
Root Mean Square (RMS) Error	0.013	0.014	0.048

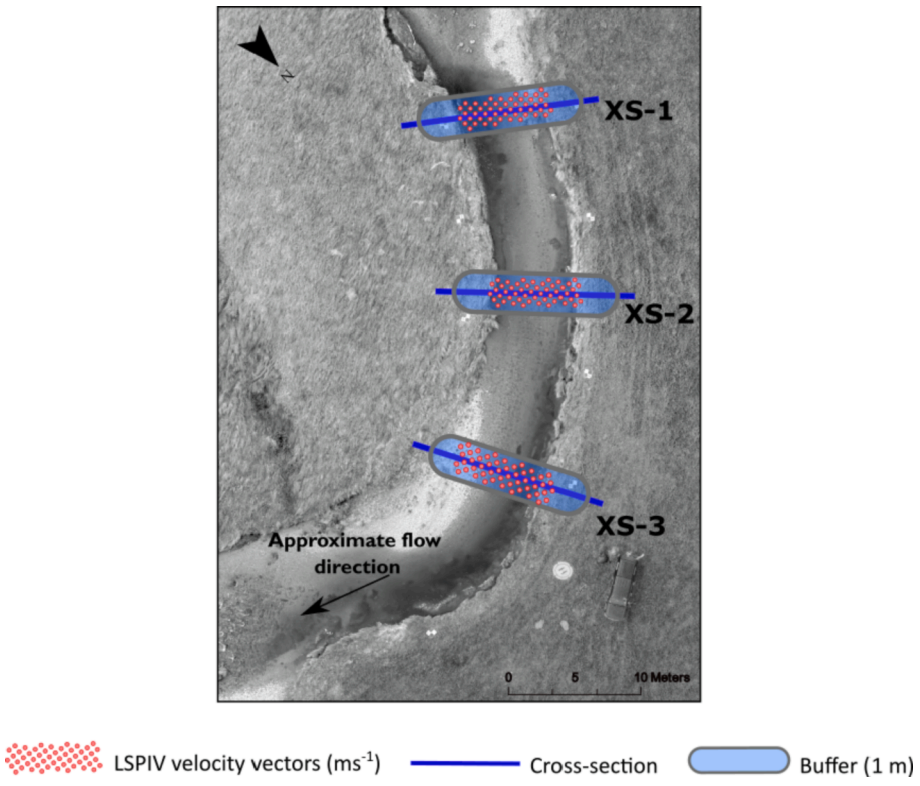

Fig. 3. Locations of cross-section velocities acquired using a current meter at sub-reach SW2.

beginning from the channel bottom to the water surface with a minimum of six (and mean of eight) individual velocities measured. This procedure was repeated from the left to the right bank of each cross-section to confirm the location of the vertical containing the maximum velocity. The vertical containing the maximum velocity at each cross-section, referred to as the *y*-axis (Fulton et al., 2020b), was then used to parametrise a Probability Concept algorithm (Chiu and Hsu, 2006) for depth-averaging of surface velocities in subsequent field experiments.

3.4. Image velocimetry (LSPIV) surface velocities

Hydraulic applications of LSPIV are based on the conventional PIV technique (Adrian, 1991), which was first modified and applied to riverine environments by Fujita et al. (1998). The computation of flow velocities in LSPIV is achieved by interrogating consecutive orthorectified images using cross-correlation algorithms (e.g., Dobson et al., 2014; Ran et al., 2016). Surface velocity is then computed by dividing the displacement of tracer particles by the time interval, Δt. LSPIV analysis yields time-averaged 2D surface velocity surfaces, which can be filtered for errors, commonly based on velocity magnitude thresholds. A comprehensive discussion of the concepts and applications of LSPIV in riverine environments is provided in Muste et al. (2008) and Tauro et al. (2017).

In this study, video sequences were acquired at select locations (Fig. 1; D-E) along the study reach using the same DJI Phantom 4 RTK UAV used in acquiring images for SfM photogrammetry. Videos were captured using the UAV's default 1″ CMOS, 20 MP camera (8.8 mm focal length) at a native resolution of 4 K (3840 × 2160) and a frame rate of 29.97 frames per second (fps) in non-RTK mode. During the field campaign, six videos were shot at a flying height of 30 m above the Swindale Beck, with a ground sampling distance (GSD) of 0.82 cm/pixel. All videos were shot at nadir with the UAV's anti-shake 3-axis gimbal countering vibration effects to deliver stable video scenes.

We processed video sub-samples of 5 min 27 *sec* (SW1) and 4 min 04 *sec* (SW2) both recorded at 30 m height. From the videos recorded during the field campaigns, a total of 856 consecutive images were extracted at a frame rate of 10 Hz. Table 2 summarizes the experimental conditions and frames used in the LSPIV analysis.

To enhance optical tracking of surface water features, which are central to the determination of surface water velocities (Pizarro et al., 2020b), we continuously introduced biodegradable Ecofoam cornstarch chips at a straight and narrow section of the stream during video recording. The displacement rate of these highly contrasting artificial tracers (also known as 'seeds'), in clear water where the channel bed was largely visible, provided a sufficiently distinct background for surface velocity computations.

3.4.1. Pivlab analysis

The open-source toolbox PIVlab (Thielicke and Stamhuis, 2014), developed in MATLAB (R2021a, MathWorks, Natick, MA, USA), was used to analyse the UAV images. The PIVlab processing workflow consists of three key stages: (1) image pre-processing; (2) image evaluation and (3) post-processing.

Individual frames from the two videos were first extracted (in PIVlab) at the frame windows detailed in Table 2. This entailed a visual inspection of the videos to identify sequences with either relatively uniform, dense seeding, or plain river flow. These respective windows were trimmed and extracted for further analysis. Although the UAV flights were conducted during favorable weather conditions, further stabilization of the extracted images was conducted in the Rectification

Table 2
LSPIV parameters adopted for the study.

Reach	Experimental Conditions	fps	Frame window	Number of frames
SW1	Seeded	10	6505–8641	214
SW1	Unseeded	10	2381–4517	214
SW2	Seeded	10	4513–6649	214
SW2	Unseeded	10	1559–3659	214

of Image Velocity Results (RIVeR) toolbox (Patalano et al., 2017) to counter residual camera movements. Stabilized images were loaded on to PIVlab for the first stage of analysis; image pre-processing.

The image pre-processing steps were conducted to enhance the appearance of tracers with respect to the background. The PIVlab algorithm applies a Contrast-limited adaptive histogram equalization (CLAHE) filter (set to 20 pixels) to enhance contrast in images. We further utilized the high pass filter to supress low frequency background information from the images, which helped emphasize particle tracers in the images.

PIVlab features two different cross-correlation algorithms for image evaluation, D-CC (single pass Direct Cross-Correlation) and FFT window deformation (Fast Fourier Transform correlation with multiple passes and deforming windows). Both techniques are based on cross correlation of small sub-images (interrogation areas, IAs) of image pairs. To estimate the correlation between image frames this study utilized FFT window deformation due to; 1) its computational efficiency (as compared to DCC), and 2) increased accuracy due to the ability to run several passes of FFT correlation on the same dataset, yielding high spatial resolution velocity vectors at a high signal–noise-ratios, according to the methodology described in Thielicke and Stamhuis (2014).

To obtain optimal parameters for LSPIV analysis, we conducted sensitivity tests on the sampling rate of image sequences and number of passes of different IA kernels in PIVlab (Figure S2). PIV analysis for all scenarios was conducted using four passes with progressively reducing IA window sizes (Table S2). Initial IA sizes were chosen based on criteria suggested by Pumo et al. (2021) considering values that were not lower than 50 % of the minimum image dimensions and higher than twice the maximum presumable frame-frame displacement. The results of this sensitivity analysis are detailed in the supplementary material (Table S3).

The width of the IAs for subsequent passes was obtained by halving the width relative to the previous pass. PIV analysis was performed with a first pass IA of 512 × 512 px, a second pass of 256 × 256 px, then 128 × 128 px, followed by 64 × 64 px all with 50 % overlap. The use of smaller IAs resulted in higher resolution vector maps, however this also increased noise and the number of erroneous correlations.

Derivatives from PIVlab are referenced to an image coordinate system whose origin is typically the top-left of the 2D plane. Calibration of the analysed images was performed to convert the analysed vector units from pixels per frame to m/s with reference to control points (GCPs) positioned using the same survey techniques used to observe the position of GCPs for SfM photogrammetry. To georeference the velocity vectors, we specified the offsets of our known co-ordinate system in PIVlab, this shifted the image coordinates and mapped them into a projected coordinate reference system (OSGB 1936/British National Grid) that was consistent with the DTM.

Post-processing of the vector fields involved a data validation process in PIVlab where erroneous vectors (outliers) were filtered using thresholds which were semi-automatically derived by comparing each velocity vector with a lower and upper threshold (horizontal velocities, *u*: −0.4 to 0.31 m s^{-1}; vertical velocities, *v:* −0.36 to 0.35 m s^{-1}). Following tests varying the standard deviation and local median filters (key determinants in the vector validation process) we arrived at values of 8 and 3 respectively for removal of outliers. Finally, residual noise in the vectors was removed by applying a data smoothing technique based on a penalized least squares method (Garcia, 2010).

3.5. LSPIV Depth-Averaged velocities

3.5.1. Surface velocity index

To convert the LSPIV surface velocity results to depth averaged velocities, a surface velocity index/coefficient (also referred to as alpha, α, in several studies (e.g., Fulton et al., 2020a; Hauet et al., 2018; Moramarco et al., 2017) was computed using a nonlinear Generalized Reduced Gradient optimization algorithm (Solver). We utilized velocities from the aDcp calibrated model (at the calibration sub reach SW1) to arrive at an appropriate theoretical depth-averaging constant. Several objective functions were used to optimize Solver in order to derive a α value, in this case; (i) a value of regression slope between the LSPIV surface velocities and (aDcp) model depth-averaged velocities that yielded a value as close to unity (1) as possible; (ii) the mean velocity difference between LSPIV and (aDcp) model velocities (a difference of ~ 0 m s^{-1}); and (iii) a mean error of ~ 0 %. The optimization algorithm referred to the gradient of each objective function as the input values changed and when the partial derivatives equalled zero, an optimum solution of the surface velocity index/coefficient was derived.

3.5.2. Probability Concept (PC)

Whilst field velocity measurements from the aDcp and the 2D model are depth averaged, LSPIV measurements represent surface flow velocities. A conventional method for transforming surface velocity, u_{surf}, to depth-averaged velocity, u_{vert} involves the use of a constant, known as a surface velocity-index (α) (e.g., Creutin et al., 2003; Le Coz et al., 2010; Legleiter and Kinzel, 2021; Tauro et al., 2017). The use of α to translate surface velocities to depth-averaged velocities is a simple yet convenient method that assumes that the vertical velocity profile is monotonous and can be characterized by a logarithmic distribution or power law (Hauet et al., 2018; Huang, 2018). The variability of published α values (0.70–0.90) at any given cross-section with stage and variations in channel geometry makes it difficult to select an appropriate value and is thus unreliable for conversion of surface velocities to mean velocities (Fulton et al., 2020b). Moreover, the use of a constant α coefficient fails to account for the dip-phenomenon (Moramarco et al., 2017), where the maximum velocity, u_{max}, occurs below the water surface due to the presence of secondary currents, resulting in $\alpha > 1$ (Fulton and Ostrowski, 2008; Fulton et al., 2020a). Dramais et al. (2011) and Welber et al. (2016) established that the principal source of error in LSPIV discharge estimates is the use of a singular α coefficient since cross-section specific values from field measurements differed significantly. This justified the acquisition of several cross-section velocity profiles in order to derive α values using the Probability Concept.

The Probability Concept, developed by Chiu (1987), is based on Shannon's Information Entropy and can be used to characterize non-standard velocity distributions where u_{max}, occurs below the water surface. The probabilistic approach provides a numerical basis for the transformation of surface velocities to depth-averaged velocities and provides a least biased two-dimensional velocity distribution that is constrained by known parameters (Marini et al., 2011). Velocity and depth data are collected to establish a *y*-axis, which is a vertical in the stream cross-section that contains the maximum surface velocity (Fulton et al., 2020a). Chiu and Hsu (2006) established that the location of the *y*-axis rarely coincides with the thalweg, is static, and insensitive to variations in flow, stage, velocity, or channel geometry.

Surface velocities measured using LSPIV were transformed to depth-averaged velocities using the PC that is based on Chiu's original velocity distribution equation (Chiu and Chiou, 1986), which maximizes entropy $f(u)$ in order to find the best velocity distribution fit. Eqs. (2) to (5) summarize the Chiu equations used, where the probabilistic velocity distribution at any point in the cross-section (*y*-axis) is represented by Equation (1):

$$u = \frac{u_{max}}{M} ln\left[1 + \left(e^{M} - 1\right) F(u)\right] \quad (1)$$

where u = velocity as a function of depth at the *y*-axis; u_{max} = maximum velocity at the *y*-axis; M = dimensionless probability parameter that describes velocity distribution; and $F(u) = \int_0^u f(u)du$ which is the cumulative distribution function, or the probability of a randomly sampled point velocity less than or equal to u. At cross-sections where u_{max} falls below the water surface, velocity distribution at the *y*-axis can be characterized by Equation (2):

$$u = \frac{u_{max}}{M} ln\left[1 + \left(e^{M} - 1\right) \frac{y}{D-h} exp\left(1 - \frac{y}{D-h}\right)\right] \quad (2)$$

where D = total distance from the channel bottom to the water surface at the y-axis, y = incremental distance from the channel bottom to the water surface, h = vertical distance from the water surface to u_{max}. An orthogonal coordinate system is used to translate the velocity distribution from probability space to physical space and is used to describe the variables h, D and y in Equation *(2)*. Where u_{max} occurs at the water surface, the velocity distribution at the y-axis is defined by Equation (3):

$$u = \frac{u_{max}}{M} ln\left[1 + \left(e^{M} - 1\right) \frac{y}{D} exp\left(1 - \frac{y}{D}\right)\right] \quad (3)$$

The probability distribution $f(u)$, M and h/D are all constant at a channel cross-section where u_{max} occurs below the water surface, LSPIV-derived surface velocities are used to estimate u_{max} assuming u is equal to uD, which is the velocity as which y equals D (Chiu and Hsu, 2006) and is represented by Equation (4):

$$u_{max} = uD \times M \times \left\{ ln\left[1 + \left(e^{M} - 1\right) \frac{1}{1 - \frac{h}{D}} exp\left(1 - \frac{1}{1 - \frac{h}{D}}\right)\right]\right\}^{-1} \quad (4)$$

The parameter φ, which is a function of M, was then derived following (Fulton et al., 2020b), using point velocities measured along the y-axis from the channel bed to the water surface. Current meter vertical velocity and depth measurements were used to compute u_{max}, M (φ), and h/D using a non-linear least-squares estimator in R v4.1.0 (R Core Team, 2013). The Gauss-Newton nonlinear least-squares method was used to solve for φ, which is a surrogate for u_{mean}/u_{max}.

3.6. 2D hydraulic modelling

The open-source Hydrologic Engineering Centre - River Analysis System (HEC-RAS version 6.0), developed by the US Army Corps of Engineers, was used to simulate depth-averaged flow conditions. Two-dimensional unsteady state flow was solved using the full momentum (Saint-Venant) equations. Despite the intensive computational demand, application of the Saint-Venant equations allowed for a detailed and accurate representation of velocity distributions (Pilotti et al., 2020) in the relatively flat mixed-flow river regime that characterizes Swindale Beck. HEC-RAS has previously been used to study channel hydraulics in a wide variety of studies (e.g., Afshari et al., 2018; Shustikova et al., 2019; Yalcin, 2020); further details on the numerical scheme are available in Brunner (2002, 2018).

3.6.1. Model configuration and calibration

A heterogenous 2D computational mesh of the Swindale Beck reach was generated, using a cell size of 5 × 5 m. HEC-RAS implements a sub-grid bathymetry approach that allows for implementation of a coarse grid on fine topographic surfaces, which saves on model computation time. To simulate fine-scale flow velocity commensurate to the resolution of measurements from the aDcp and image velocimetry, the spatial resolution of the computational reach was refined to 0.5 × 0.5 m between the channel banks by enforcing a break-line running along the thalweg.

A discharge hydrograph from the United Utilities gauging station was used as the inflow boundary condition, with flow scaled (by a factor of 0.9) to the catchment size, since the actual gauging station was located 650 m downstream from the upstream boundary. An energy slope gradient, equivalent to the normal depth, was estimated by computing the bed slope along the terrain profile. The energy slope value was used as the outflow boundary condition, situated downstream of the computational mesh. To avoid errors arising from downstream backwater effects and upstream velocity distributions, the boundaries were located appropriately downstream from the domain of interest.

The 2D model was calibrated at sub-reach SW1 for both the aDcp model (hereinafter referred to as model M_{aDcp}) and the LSPIV model (hereinafter referred to as model M_{LSPIV}) by adjusting a spatially discretized manning's roughness coefficient n and eddy viscosity coefficients until model simulations closely matched observed (aDcp and LSPIV) velocities (Fig. 4). Model simulations were calibrated by varying a spatially discretized Manning's roughness coefficient, n, whilst keeping the n of the overbank zones constant at 0.035. We further calibrated the models using the eddy viscosity terms by turning on HEC-RAS's turbulence mixing coefficients. Since eddy viscosity in HEC-RAS's numerical scheme is computed as the sum of the Longitudinal Mixing Coefficient D_L, the Transverse Mixing Coefficient D_T and the dimensionless Smagorinsky Coefficient C_s, these mixing parameters were calibrated to the spatially distributed aDcp (model M_{aDcp}) and LSPIV velocities (model M_{LSPIV}). The conservative turbulence model formulation, which ensures little to no momentum loss, was utilized., Variable-time step control using the Courant-Friedrichs-Lewy condition was used to ensure model stability and better model velocity distributions.

3.6.2. Calibration/Validation performance assessment

LSPIV and aDcp observed velocities were compared to the model simulation runs, with the aDcp calibrated model (model M_{aDcp}) serving as an initial benchmark of minimum validation performance indicators. Whilst there are no set standards for 2D model performance assessment, Pasternack (2011) proposed a rigorous suite of metrics, which can be used to assess 2D model validation performance. Complemented with some of the hydrological validation metrics presented by Moriasi et al. (2007) and Biondi et al. (2012), most of the uncertainty in 2D shallow-water models can be quantified. Thus the assessment metrics used were: (i) regression analysis evaluating the slope of the regression line between observed versus predicted velocities, the y-intercept, regression slope standard error, regression intercept standard error and the coefficient of determination, R^2; (ii) hydrological performance metrics; Nash-Sutcliffe efficiency (NSE), percent bias (PBIAS) and ratio of the root mean square error to the standard deviation of observations (RSR); (iii) error statistics; Mean Absolute Error (MAE), Root Mean Square Error (RMSE), Standard Deviation of Error (SDE) and the Mean Absolute Percentage Error (MAPE).

4. Results

The results are presented as follows: First, we report the 2D model calibration results at sub-reach SW1 using a subset of aDcp data, which formed the benchmark for field velocity observations (model M_{aDcp}) (Section 4.1). Results of a separate model similarly calibrated at SW1 using LSPIV surface velocity data (model M_{LSPIV}) are then presented (Section 4.1). This is followed by results from the validation model M_{aDcp} using aDcp data at sub-reach SW2 (Section 4.2.1). Results of the validation performance of model M_{LSPIV} using LSPIV surface velocities, depth-averaged using a spatially constant theoretical coefficient (referred to as $LSPIV_{\alpha}$) are then presented (Section 4.2.2). Further detailed results of the validation of model M_{LSPIV} velocity simulations are reported, based on a sub-set of LSPIV surface velocities within a 1 m distance of three field cross-sections, all depth-averaged using the Probability Concept (hereinafter referred to as $LSPIV_{PC}$) (Section 4.2.3).

4.1. 2D model calibration

A sensitivity analysis of the appropriate bed roughness, based on previous modelling studies using HEC-RAS (e.g., Shustikova et al.,2019), set starting n values in the range of 0.025 to 0.033 and was adjusted by 0.002 increments to a final value of 0.030 (model M_{aDcp}) and 0.032 (model M_{LSPIV}). Eddy viscosity is computed as the sum of the longitudinal (D_L), transverse (D_T) and Smagorinsky coefficients (dimensionless, C_s) in the HEC-RAS numerical modelling scheme. Fig. 4 shows the calibrated model velocity predictions for sub-reach SW1 using the aDcp and LSPIV datasets.

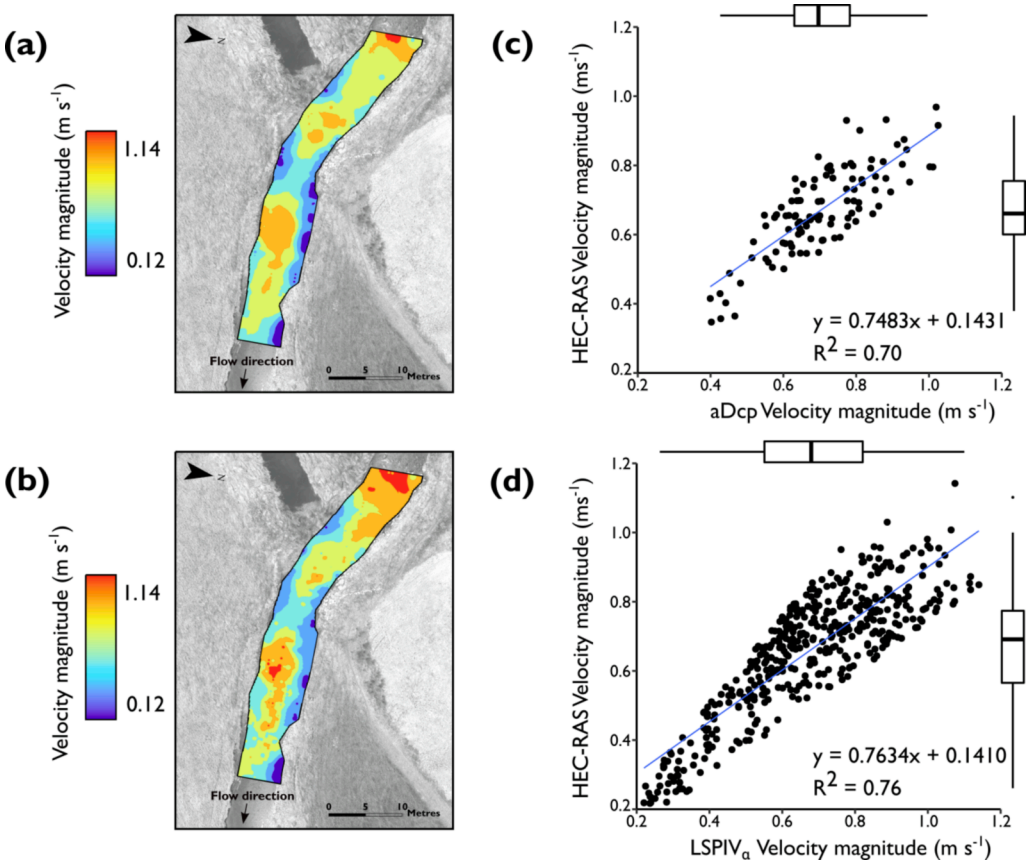

Fig. 4. Calibration results of 2D model simulations at sub-reach SW1. Model M_{aDcp} (a) and model M_{LSPIV} (b) velocity predictions. Scatter plots of aDcp (c) and $LSPIV_{\alpha}$ (d) velocity observations versus model predictions. (In the box plots, the boundary of the box closest to zero indicates the 25th percentile, the black line within the box marks the median, and the boundary of the box farthest from zero indicates the 75th percentile. Points above or below the plots indicate outliers outside the 10th and 90th percentiles).

Simultaneously adjusting the turbulence mixing and dispersion parameters yielded final values of $D_L = 1$, $D_T = 0.3$ and $C_s = 0.05$ for model M_{aDcp} and; $D_L = 1.4$, $D_T = 0.26$ and $C_s = 0.03$ for model M_{LSPIV} with both parameterisations yielding the lowest errors in the distribution of modelled velocities. Computational grid sizes were discretized for the channel and floodplain, with a refined grid size of 0.5 m in-channel and 5 m for the rest of the floodplain yielding optimum model performance.

Table 3 shows the error analysis results from the calibrated models. Higher precision of all benchmarks was observed when the river's flow was seeded versus when left unseeded. These results are corroborated by other studies, such Pearce et al. (2020), Dal Sasso et al. (2021a,b) and Liu et al. (2021) who showed that the LSPIV algorithm performs better when tracers (which are important for mapping flow fields between image frames), whether natural or artificial, are abundant on the water surface. Because of the drastic drop in most assessment benchmarks when using the unseeded flow scenario to calibrate the 2D hydraulic model (most notably bias (13.2 %), and R^2 (37.5 %)) we used only the seeded runs for model calibration. The uncertainty associated with insufficient seeding is discussed (Section 5.2.1).

4.2. 2D model validation

4.2.1. aDcp model validation

aDcp data were used to validate the 2D model at sub-reach SW2 (Fig. 5) and set a benchmark for comparison with model M_{LSPIV} which was fully calibrated and validated using LSPIV velocity fields. Results from the aDcp model validation are detailed in Table 3, with a final R^2 of 0.70 and slope of 0.85.

Similar studies (e.g., Gard, 2008; Lane et al., 1999; Pasternack et al., 2006) have reported R^2 of predicted versus modelled velocity values ranging from 0.4 to 0.99 with slopes between 0.6 and 1. The results from this study were in the upper range of published results. The hydrological performance indicator NSE yielded an acceptable value at 0.67 with a PBIAS of 0.13 %. This shows the 2D model tended towards an

Table 3
2D model calibration/validation metrics for Models M_{aDcp} and M_{LSPIV}.

	Model M_{aDcp}			Model M_{LSPIV}	
	Calibration (aDcp)	Validation (aDcp)	Seeded Calibration ($LSPIV_{\alpha}$)	Unseeded Calibration ($LSPIV_{\alpha}$)	Seeded Validation ($LSPIV_{\alpha}$)
R^2	0.70	0.70	0.76	0.52	0.75
NSE	0.65	0.67	0.75	0.23	0.76
PBIAS	−4.76 %	0.13 %	−2.48 %	10.71 %	0.02 %
MAE, m/s	0.07	0.06	0.09	0.13	0.09
RSR	0.59	0.58	0.49	0.87	0.50
Trendline Slope	0.74	0.85	0.76	0.82	0.75
Regression Slope Standard Error	0.0463	0.0401	0.0204	0.0395	0.0199
Regression Intercept Standard Error	0.0332	0.0189	0.0143	0.0208	0.0137
n	112	196	445	410	461

Note. R^2 = coefficient of determination; NSE = Nash-Sutcliffe efficiency; PBIAS = percent bias; RMSE = root mean square error; MAE = Mean absolute error, SD = standard deviation; RSR = ratio of the root mean square error to the standard deviation of observed data; *n* = number of observations.

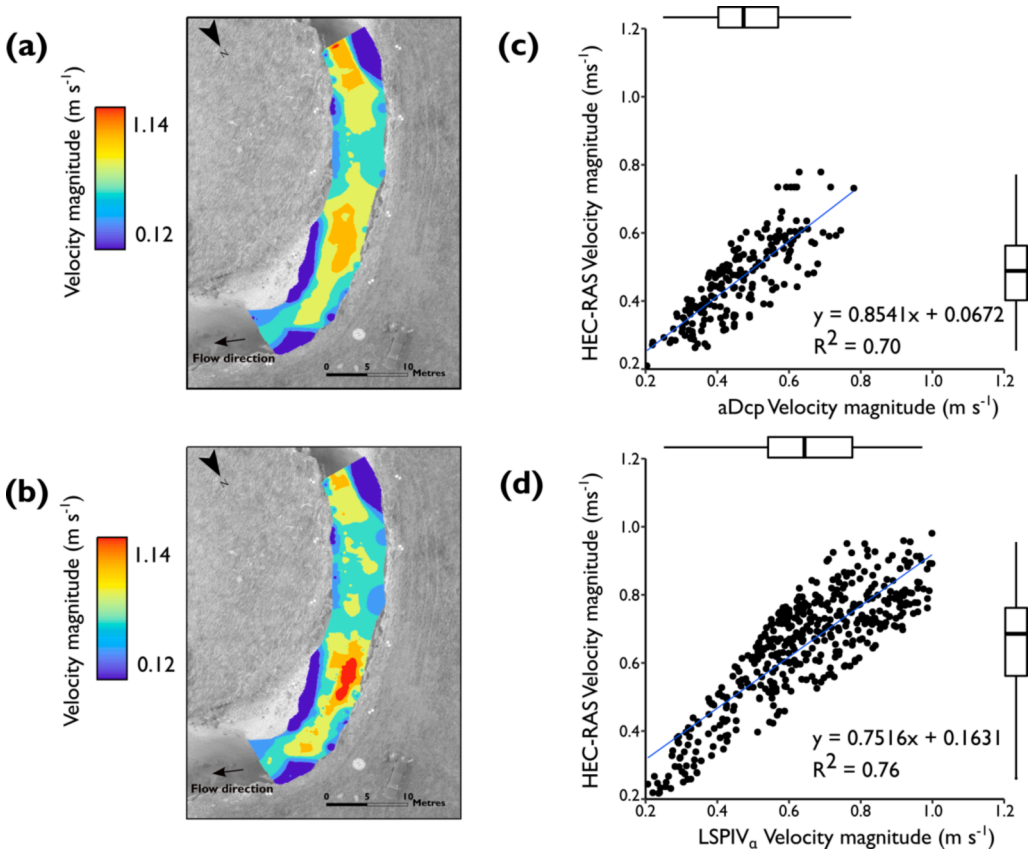

Fig. 5. Validation results of 2D model simulations at sub-reach SW2. Model M_{aDcp} (a) and model M_{LSPIV} (b) velocity predictions. Scatter plots of aDcp (c) and $LSPIV_{\alpha}$ (d) velocity observations versus model predictions.

overestimation bias, with high velocity values being underpredicted whilst low values were overpredicted, similar to the findings of Barker et al. (2018).

4.2.2. $LSPIV_{\alpha}$ model validation

Model M_{LSPIV} (calibrated using LSPIV data) was validated against all the performance metrics used to evaluate the validation performance of model M_{aDcp}. A surface velocity index (α) of 0.89 (derived using the method described in Section 3.5.1) was used to depth average the LSPIV velocities at SW2, further optimising the validation results. Referencing the standard error of the regression slope, Model M_{LSPIV} had a validation error magnitudes half that of Model M_{aDcp}. A PBIAS value of 0.02 % indicated a slight model overestimation bias, which is consistent with the findings of Liu et al. (2021) and can also be attributed to the use of a singular coefficient (α) to transform surface velocities to depth-averaged velocities.

Overall, there was a strong correlation between modelled velocities and $LSPIV_{\alpha}$ velocities with a R^2 value of 0.75 and slope of 0.75. These high correlation values can be attributed to not only the quality of the model, but also the abundance of LSPIV observations which enabled the full statistical structure of the correlation to be revealed, as opposed to having fewer validation points which would tend to be biased to low or intermediate velocities.

4.2.3. $LSPIV_{PC}$ model validation

Different from the initial validation of the model M_{LSPIV}, which relied on a theoretical constant (α) to translate LSPIV surface velocities to depth averaged velocities, a probability-based cross-sectional validation of the model was carried out using the Probability Concept to further understand LSPIV's performance (referred to as $LSPIV_{PC}$) in 2D model validation. Three cross-sections (Fig. 3) were collected at sub-reach SW2 using an EM flow meter and vertical velocity profiles sampled at these locations were used to compute φ, following which LSPIV velocity vectors within a 1 m range of the respective cross-sections were extracted for further model validation.

Values of φ, which is constant at any cross-section and used to transform u_{max} to u_{mean}, ranged from 0.571 to 0.658, which is consistent with previously published work (Chiu and Hsu, 2006; Fulton et al., 2020b, 2018; Moramarco et al., 2017) where values ranging from 0.522 to > 1 have been reported. Table 4 shows the velocity distributions at the *y-axis* for each cross-section of interest, which was established through repeat current-meter wading measurements.

Goodness-of-fit statistics (Table 5) showed the model was validated with correlations outperforming the $LSPIV_{\alpha}$ validation results for all but one cross-section (XS-1), which was located slightly downstream of a riffle bend making it susceptible to well documented turbulence-closure uncertainties at such points (Barker et al., 2018). R^2 correlation values

Table 4
Probability-Concept-derived metrics and velocities measured using a Valeport electromagnetic current meter at three cross-sections along the Swindale Beck (M = dimensionless parameter characterizing velocity distribution; φ = a function of M equal to the ratio of the mean velocity to the maximum velocity; u_s = surface velocity in m/s; u_{max} = maximum velocity; *y*-axis = vertical depth in a cross-section that contains the maximum velocity in metres, m).

Cross-section	Probability-Concept Metrics				
	M (dim)	Φ (dim)	U_s (m/s)	u_{max} (m/s)	Water depth at *y*-axis (m)
XS-1	0.325	0.571	0.493	0.493	0.14
XS-2	1.169	0.595	0.053	0.053	0.29
XS-3	0.478	0.539	0.041	0.041	0.35

Table 5
Velocity magnitude validation metrics comparing $LSPIV_{PC}$ velocities versus HEC-RAS (modelled) velocities.

Cross-section	$LSPIV_{PC}$ Validation Metrics					
	R^2	NSE	PBIAS	Trendline Slope	RS. Standard Error	RI. Standard Error
XS-1	0.73	0.67	6.42 %	0.91	0.1471	0.0423
XS-2	0.81	0.81	0.91 %	0.73	0.0843	0.0310
XS-3	0.78	0.68	3.74 %	1.04	0.0656	0.0206

ranged from 0.73 to 0.81 (Fig. 6a), despite the reduction in data points used to evaluate 2D model performance, indicating that φ represented an appropriate velocity distribution unique to each profile. PBIAS values revealed a bias in which higher velocity values were underestimated by $LSPIV_{PC}$ and lower values overestimated, similar to the findings of Pasternack et al. (2006), indicating the 2D model less accurately reproduced the highest and lowest flows in the channel.

Velocity magnitude correlations between modelled and observed ($LSPIV_{PC}$) velocities closely tied to 1:1 linearity with regression slopes ranging from 0.73 to 1.04 (Table 5) following conditioning of the regression slope at each section using φ, these results are well within peer-reviewed studies of 2D model validation (Barker et al., 2018; Pasternack et al., 2006). Comprehensive scatterplot analysis when validating a 2D model using velocity magnitude should also include results of zero intercept values, which were suggested by Pasternack et al. (2006) to be < 5 % of maximum velocity. All regression zero intercept values were well below this threshold.

Mean absolute $LSPIV_{PC}$ velocity magnitude error (as compared to calibrated model results) across all cross-sections was less than the 15–30 % benchmark suggested by Pasternack, (2011), with the highest value being 24.35 %, while the highest median error was 24.01 % (Fig. 6b). The negative mean velocity differences, following depth averaging using φ at each cross-section, can all be explained by the fact that most velocity values were quite low (<0.5 m s^{-1}) yet the model typically overpredicted low velocities. Percent rank analysis of all deviations revealed that 98 % of the velocity values had error<50 %, with outliers falling within a maximum error bin of 75 %. Further, mean errors from using $LSPIV_{PC}$ velocities for model validation reduced by 7.7 % as compared to depth averaging using a single constant (α) (Fig. 6c).

The histogram analysis of error distributions (Fig. 7) revealed that 98.2 % of the data from $LSPIV_{PC}$ cross sectional validation had an error of 50 % or less. The mean absolute velocity error across all sections was 16.86 % with error peaks observed at XS-3 where 94.4 % of the data had errors of 35 % or less.

5. Discussion

5.1. Advanced sampling of spatial velocity distributions

The calibration and validation of a 2D model using both

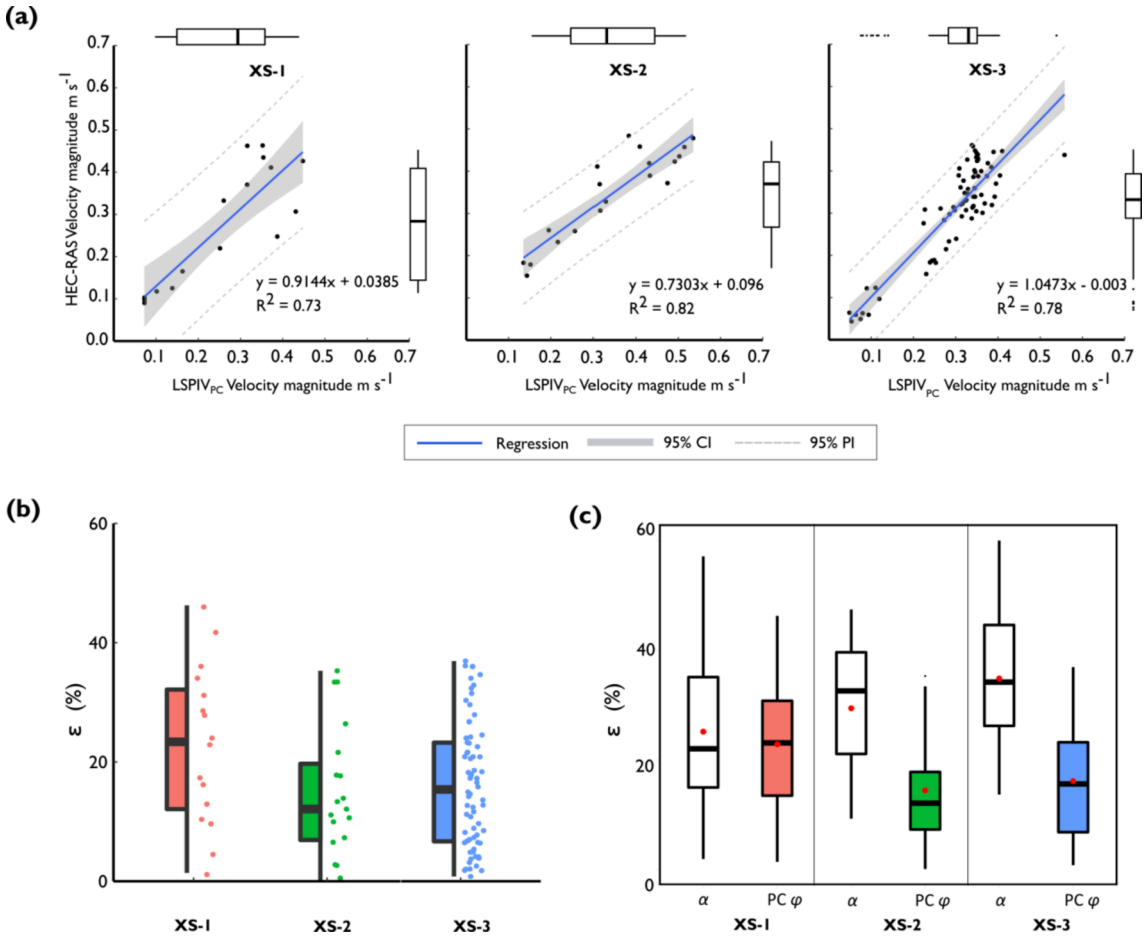

Fig. 6. (a) Scatter plots of $LSPIV_{PC}$ vs HEC-RAS velocity magnitudes with linear regression fits, 95% confidence (CI) and prediction (PI) intervals; (b) Variation in absolute $LSPIV_{PC}$ velocity error (ε) as compared to modelled velocities across the six cross-sections. Individual velocity error observations are represented by the coloured dots. Horizontal line in the boxplot indicates the median, box shows the interquartile range (IQR), and the whiskers are 1.5*IQR; (c) Absolute percentage errors (ε) in estimating depth-averaged velocity using the standard velocity index (α, white) and the Probability Concept approach (PC, φ) at cross-sections XS1 – 3 (red dot indicates mean error). (For interpretation of the references to colour in this figure legend, the reader is referred to the web version of this article.)

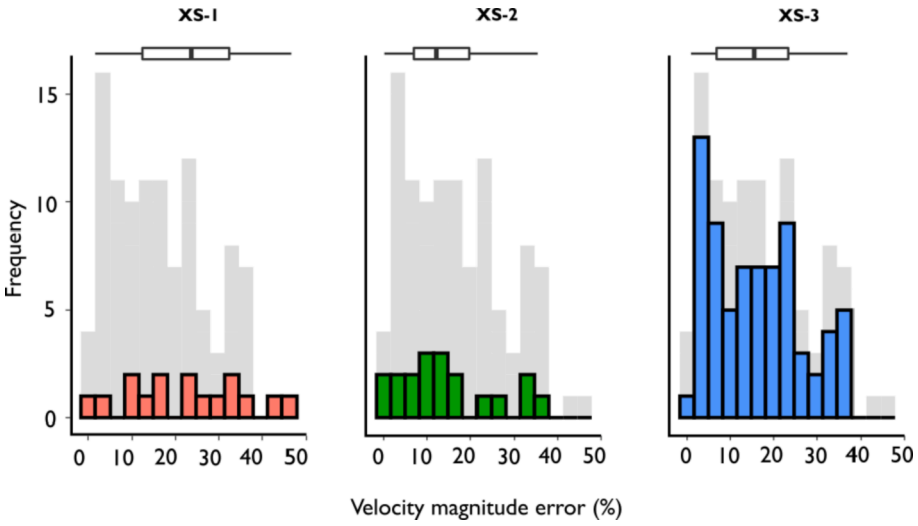

Fig. 7. Velocity magnitude error histograms for all $LSPIV_{PC}$ cross-sections (relative to model M_{LSPIV} predictions) with overall error in the background (grey).

conventional aDcp and LSPIV velocities was demonstrated, with the performance of the model fully calibrated/validated using LSPIV data being on par with results reported in peer-reviewed literature (Table 3, 4). With both approaches yielding valid performance, discussion focuses on the additional novelties introduced by using LSPIV surface velocity datasets combined with the Probability Concept (PC) for derivation of a velocity depth-averaging index (φ).

Although field measurements of velocity using aDcps can be achieved for depths $>$ 80 m (e.g., Sontek's M9), the impracticality of deploying them in very fast and deep waters precludes their ability to sample very high velocity events. Further, aDcps cannot be operated in very shallow rivers due to the instrument's blanking distance. In contrast, the capability of LSPIV to sample a boarder range of velocities allowed for the collection of previously unattainable velocity data. Statistical analyses of the results revealed the first key novelty of this study, which was the remarkable improvement in model validation performance when using (seeded) LSPIV to parametrise a 2D model instead of aDcp data. Plotting $LSPIV_{PC}$ velocities against model results yielded coefficient of determination values (R^2) of between 0.73 and 0.81, which was up to 10 % better when compared to the model fully parametrised using aDcp data (M_{aDcp}), and among the highest values reported in peer-reviewed literature for direct velocity magnitude validation of 2D models (e.g., Barker et al., 2018; Fischer et al., 2015; Gard, 2008). A statistical explanation offers insight into this high performance; with the ability of LSPIV to sample and obtain a wide range and distribution of velocities (as compared to the aDcp), a better characterization of the spatial patterns of velocity was available for analysis. In addition, the number of LSPIV observations, which was several orders of magnitude higher than that of the aDcp at both sub-reaches, helped reveal the full statistical structure of the correlations as opposed to having fewer observations which would tend to be biased to either low or intermediate velocities. As suggested by Pasternack (2011), an appropriate benchmark for determining whether a model has been validated, based on velocity simulations, should be centred on the magnitude of measurements observed as the greater the number of observations, the better the spread of velocity distributions and the resultant R^2 correlations.

Departing from the well-established method of using selected cross-sections to validate 2D models, we successfully validated model performance across a wider range of velocities spanning varying morphological structures, which are typically left out in velocity validation studies. The LSPIV surface velocity measurements were generally in very good agreement with the model simulations which can partly be attributed to the rather shallow depth and high gradient of the gravel bed channel. Given these hydraulic settings, the accuracy of LSPIV velocities tended to be higher than the aDcp's, which depends on extrapolation of the top and bottom subsections of the channel to compute velocities. Similar to an earlier study by Baird et al. (2021), the 2D model overpredicted high velocities and underpredicted low velocities in both modelling scenarios, underlining the added benefit of LSPIV that sampled a significantly wider range of velocity bins for a robust analysis of the 2D model's performance. The spatially dense coverage of LSPIV not only captured the diversity and transitions of low-flow velocity fields but presented the possibility for mapping surface velocities in high flow, steep channel sections where bankfull flow conditions could typically have ruled out model validation using aDcp observations due to physical inaccessibility (e.g. Abu-Aly et al., 2014; Sawyer et al., 2010).

5.2. Uncertainty

5.2.1. Uncertainty of LSPIV surface velocity measurements

The accuracy of image velocimetry techniques in field conditions is heavily influenced by the ability to identify and track surface features, which are central in the computation of surface velocity (Dal Sasso et al., 2021b; Pizarro et al., 2020a; Tauro et al., 2017). Recent studies by Pizarro et al., 2020b) introduced a tracer seeding metric known as the seeding distribution index (SDI) in an attempt to identify the optimal spatial distribution of tracers. However, the errors computed using all the image frames from their study were not different from the optimal window suggested by the SDI. Therefore, the experimental settings adopted in this study focused on the overall performance of natural/unseeded velocity estimates versus seeded estimates in assessing spatial velocity outputs from the 2D model.

Field experiments using artificial seed tracers had better model calibration performance across all assessment metrics when compared to unseeded scenarios (Table 3). The coefficient of determination (R^2) dropped by 37.5 % when the flow was left unseeded. This reduction in collinearity between simulated (model) and observed (LSPIV) data for the unseeded scenarios was unsurprising as the magnitude and spatial distribution of the u and v components of velocity magnitude tended to dramatically decline. The NSE results further underlined the strong influence of seeding on the reliability of LSPIV results, with differences of up to 50 % in the residual variance in velocity compared to the measured variance. These results are consistent with the findings of Pearce et al. (2020) who observed a high sensitivity of LSPIV to seeding density when assessing aDcp velocities. Although the reliability of LSPIV results diminishes dramatically under unseeded conditions, Naves et al. (2021) demonstrated that the presence of bubbles caused by raindrops could

positively influence cross-correlation algorithms. This implies future scope for the application of these methods during flooding events, which are typically accompanied by heavy rainstorms.

5.2.2. Variability in velocity coefficient, α

The accurate derivation of a velocity coefficient, α, which represents the ratio of surface velocity to depth-averaged velocity remains a key source of uncertainty in the use of non-contact methods to compute mean channel velocities (Dal Sasso et al., 2021a). Dramais et al. (2011) identified the variability of α as the dominant source of error when using LSPIV to compute velocity estimates, recommending the derivation of site-specific α values. To the best of our knowledge, previously published studies have generally utilised the standard value of α (0.85), assuming a logarithmic vertical velocity distribution (e.g., Le Coz et al., 2010, Lewis et al., 2018), or derivation of a power-law exponent (e.g., Johnson and Cowen, 2017) when translating surface velocities to depth-averaged velocities. The variability of φ in gravel bed rivers has been reported to be larger (Lee and Julien, 2006) further suggesting the requirement for locally calibrated α values. Moreover, α values derived assuming a monotonous velocity distribution fail to account for the 'dip phenomenon', where maximum flow velocity, u_{max} occurs below the water surface resulting in $\alpha > 1$.

Using Chiu's PC (Chiu, 1987), which is based on Shannon's Information Entropy (Shannon, 1948), we successfully computed α at three cross-sections within the study sub-reaches. The entropy method showed marked variability in α across XS1-3 (Table 4), with analysis showing that our results were on the lower end of published values (0.539–0.658). Whilst the use of cross section specific α in depth averaging LSPIV values had no impact the coefficient of determination (R^2) tests, there was a notable trend in the improvement of other validation metrics such as the best-fit trendline slope (i.e., slope tending towards 1) and the values of regression slope standard error and regression intercept standard error all improving substantially.

Results from our study propose that the use of default values of α is insufficient in gravel bed rivers, likely due to the influence of bed roughness, as suggested by Hauet et al. (2018). We suggest that probabilistically derived values of α yield better estimates of depth-averaged LSPIV velocity with the ability to account for the dip-phenomenon. Overall, we find that the use of locally derived α using Chiu's (Chiu, 1987) probability function more accurately constrains velocity bias at all cross-sections (Table 5) with average errors of 27.73 % (Probability Concept, φ) and 18.90 % (α) indicating a 37.9 % improvement in velocity predictions. These findings are expected and corroborated by other studies such as Moramarco et al. (2017). The median error did not exceed 24 % and 34 % for the Probability Concept and velocity index methods respectively with the 95th percentile of errors at every cross-section being lower when assuming a non-logarithmic velocity distribution. Our field experiments show that using alternative velocity distribution approaches provides better fits of depth-averaged velocity profiles than reliance on theoretical *a priori* indices commonly used in several studies. Further research is necessary to ascertain the variability of φ with different discharges as well as its dependence on cross-sectional distancing.

6. Conclusion

This investigation has shown that a 2D hydraulic model can be accurately calibrated and validated using image velocimetry data, yielding results comparable to traditional aDcp approaches. Further, we established that the uncertainty commonly associated with depth-averaging surface flows in standard LSPIV workflows can be significantly reduced using numerical methods, based on the channel's hydraulic parameters (φ, y-axis, u_{max}) rather than relying on the often-used constants or indices based on an assumption of logarithmic velocity distributions in channels. The use of probabilistically derived φ for surface velocity averaging resulted in error reductions of up to 7.7 % when validating a hydraulic model; however, the Probability Concept approach does require in-channel cross-section measurements to obtain y-axis (profile with maximum velocity) data. To the authors' knowledge, the joint deployment of LSPIV with the Probability Concept for estimation of depth-averaged channel velocities in assessing simulated flows in a natural gravel bed river has not been demonstrated previously. This study allowed two other significant conclusions to be reached. First, whilst image velocimetry and aDcp yielded comparable model performance, the greater size of the LSPIV dataset, which spanned a wider range of flows and depths, allowed for the full statistical structure of field measurements to be revealed. However, the limitations of LSPIV-derived surface velocity fields were clear in conditions where there is sparse seeding on water surfaces or in poorly illuminated conditions. Whilst this assessment is not a direct comparison between LSPIV and aDcp observations, it demonstrates the capabilities of LSPIV in deriving meaningful data that can be used to calibrate and validate 2D models. Second, and more broadly, the use of high-quality datasets to validate model performance is key for the reduction in uncertainty in model predictions. The overall reduction in error distributions and low bias during model validation demonstrates that LSPIV, coupled with the PC, is a fit for purpose tool in evaluating reach-scale hydraulic model predictions.

CRediT authorship contribution statement

Christopher Masafu: Conceptualization, Methodology, Formal analysis, Investigation, Data curation, Writing – original draft, Visualization. **Richard Williams:** Conceptualization, Methodology, Investigation, Writing – review & editing, Supervision. **Xiaogang Shi:** Conceptualization, Writing – review & editing, Supervision. **Qiangqiang Yuan:** Conceptualization, Writing – review & editing, Supervision. **Mark Trigg:** Writing – review & editing.

Declaration of Competing Interest

The authors declare that they have no known competing financial interests or personal relationships that could have appeared to influence the work reported in this paper.

Acknowledgements

The authors thank Dr Mathew Perks, the two anonymous reviewers, and the editor for their constructive and valuable comments. Thanks to Kenny Roberts and Craig MacDonell for piloting UAV surveys and field assistance; Lee Schofield of Swindale Beck for access to the study site; United Utilities for supply of hydrometric data; Christopher Mason (USGS) and Sophie Pearce for valuable assistance with image velocimetry algorithms.

Author Contributions

Conceptualization, C.M., R.D.W., X.S. and Q. Y.; methodology, C.M., R.D.W.; formal analysis, C.M.; investigation, C.M, R.D.W.; data curation, C.M.; writing—original draft preparation, C.M.; writing—review and editing, R.D.W., X.S., Q. Y. and M.T.; visualization, C.M.; supervision, X. S., R.D.W., and Q. Y. All authors have read and agreed to the published version of the manuscript.

Data access

Observation and model data are available through the University of Glasgow's Enlighten repository here: https://doi.org/10.5525/gla.researchdata.1325.

Funding

CM was funded by the Lord Kelvin Adam Smith (LKAS) PhD scholarship at the University of Glasgow. GNSS equipment was provided by Natural Environment Research Council's Geophysical Equipment Facility (NERC GEF) loan 1118.

Appendix A. Supplementary data

Supplementary data to this article can be found online at https://doi.org/10.1016/j.jhydrol.2022.128217.

References

Abu-Aly, T.R., Pasternack, G.B., Wyrick, J.R., Barker, R., Massa, D., Johnson, T., 2014. Effects of LiDAR-derived, spatially distributed vegetation roughness on two-dimensional hydraulics in a gravel-cobble river at flows of 0.2 to 20 times bankfull. Geomorphology 206, 468–482. https://doi.org/10.1016/j.geomorph.2013.10.017.

Adrian, R.J., 1991. Particle-imaging techniques for experimental fluid mechanics. Annu. Rev. Fluid Mech. 23, 261–304. https://doi.org/10.1146/annurev.fl.23.010191.001401.

Afshari, S., Tavakoly, A.A., Rajib, M.A., Zheng, X., Follum, M.L., Omranian, E., Fekete, B. M., 2018. Comparison of new generation low-complexity flood inundation mapping tools with a hydrodynamic model. J. Hydrol. 556, 539–556. https://doi.org/10.1016/j.jhydrol.2017.11.036.

Al-mamari, M., Kantoush, S., Kobayashi, S., Sumi, T., Saber, M., 2019. Real-time measurement of flash-flood in a wadi area by LSPIV and STIV. Hydrology 6, 27. https://doi.org/10.3390/hydrology6010027.

Amelinckx, S., 1971. Classical dynamics of particles and systems. Phys. Bull. 22, 157–158. https://doi.org/10.1088/0031-9112/22/3/020.

Annis, A., Nardi, F., Petroselli, A., Apollonio, C., Arcangeletti, E., Tauro, F., Belli, C., Bianconi, R., Grimaldi, S., 2020. UAV-DEMs for small-scale flood hazard mapping. Water 12, 1717. https://doi.org/10.3390/w12061717.

Baird, D., Abban, B., Scurlock, S., Abt, S., Thornton, C., 2021. Two-dimensional numerical modeling of flow in physical models of rock vane and bendway weir configurations. Water 13, 458. https://doi.org/10.3390/w13040458.

Barker, J.R., Pasternack, G.B., Bratovich, P.M., Massa, D.A., Wyrick, J.R., Johnson, T.R., 2018. Kayak drifter surface velocity observation for 2D hydraulic model validation. River Res. Appl. 34, 124–134. https://doi.org/10.1002/rra.3238.

Bechle, A.J., Wu, C.H., 2014. An entropy-based surface velocity method for estuarine discharge measurement. Water Resour. Res. 50, 6106–6128. https://doi.org/10.1002/2014WR015353.

Bernhofen, M.V., Whyman, C., Trigg, M.A., Sleigh, P.A., Smith, A.M., Sampson, C.C., Yamazaki, D., Ward, P.J., Rudari, R., Pappenberger, F., Dottori, F., Salamon, P., Winsemius, H.C., 2018. A first collective validation of global fluvial flood models for major floods in Nigeria and Mozambique. Environ. Res. Lett. 13, 104007 https://doi.org/10.1088/1748-9326/aae014.

Biondi, D., Freni, G., Iacobellis, V., Mascaro, G., Montanari, A., 2012. Validation of hydrological models: Conceptual basis, methodological approaches and a proposal for a code of practice. Phys. Chem. Earth Parts A/B/C 42–44, 70–76. https://doi.org/10.1016/j.pce.2011.07.037.

Brunner, G.W., 2002. Hec-ras (river analysis system), in: North American Water and Environment Congress & Destructive Water. ASCE, pp. 3782–3787.

Brunner, G.W., 2018. Benchmarking of the HEC-RAS Two-Dimensional Hydraulic Modeling Capabilities.

Brunner, G.W., United States., Army., Corps of Engineers., Institute for Water Resources (U.S.), Hydrologic Engineering Center (U.S.), 2020. HEC-RAS river analysis system : hydraulic reference manual. US Army Corps of Engineers, Institute for Water Resources, Hydrologic Engineering Center, Davis, CA.

Cao, L., Weitbrecht, V., Li, D., Detert, M., 2021. Airborne Feature Matching Velocimetry for surface flow measurements in rivers. J. Hydraul. Res. 59 (4), 637–650.

Carrivick, J.L., Smith, M.W., 2019. Fluvial and aquatic applications of Structure from Motion photogrammetry and unmanned aerial vehicle/drone technology. WIREs Water 6, e1328.

Cea, L., Legout, C., Darboux, F., Esteves, M., Nord, G., 2014. Experimental validation of a 2D overland flow model using high resolution water depth and velocity data. J. Hydrol. 513, 142–153. https://doi.org/10.1016/j.jhydrol.2014.03.052.

Chiu, C., 1987. Entropy and probability concepts in hydraulics. J. Hydraul. Eng. 113, 583–599. https://doi.org/10.1061/(ASCE)0733-9429(1987)113:5(583).

Chiu, C., Chiou, J., 1986. Structure of 3-D Flow in rectangular open channels. J. Hydraul. Eng. 112, 1050–1067. https://doi.org/10.1061/(ASCE)0733-9429(1986)112:11(1050).

Chiu, C.-L., Hsu, S.-M., 2006. Probabilistic approach to modeling of velocity distributions in fluid flows. J. Hydrol. 316, 28–42. https://doi.org/10.1016/j.jhydrol.2005.04.011.

Creutin, J.D., Muste, M., Bradley, A.A., Kim, S.C., Kruger, A., 2003. River gauging using PIV techniques: a proof of concept experiment on the Iowa River. J. Hydrol. 277, 182–194. https://doi.org/10.1016/S0022-1694(03)00081-7.

Dal Sasso, S.F., Pizarro, A., Manfreda, S., 2021a. Recent advancements and perspectives in UAS-Based image velocimetry. Drones 5, 81. https://doi.org/10.3390/drones5030081.

Dal Sasso, S.F., Pizarro, A., Pearce, S., Maddock, I., Manfreda, S., 2021b. Increasing LSPIV performances by exploiting the seeding distribution index at different spatial scales. J. Hydrol. 598, 126438 https://doi.org/10.1016/j.jhydrol.2021.126438.

DeBell, L., Anderson, K., Brazier, R.E., King, N., Jones, L., 2016. Water resource management at catchment scales using lightweight UAVs: current capabilities and future perspectives 4, 24.

Dobson, D.W., Todd Holland, K., Calantoni, J., 2014. Fast, large-scale, particle image velocimetry-based estimations of river surface velocity. Comput. Geosci. 70, 35–43. https://doi.org/10.1016/j.cageo.2014.05.007.

Dramais, G., Le Coz, J., Camenen, B., Hauet, A., 2011. Advantages of a mobile LSPIV method for measuring flood discharges and improving stage–discharge curves. J. Hydro-environ. Res. 5, 301–312. https://doi.org/10.1016/j.jher.2010.12.005.

Eltner, A., Sardemann, H., Grundmann, J., 2019. Flow velocity and discharge measurement in rivers using terrestrial and UAV imagery. Hydrol. Earth Syst. Sci. Discuss. 1–29 https://doi.org/10.5194/hess-2019-289.

Eltner, A., Sardemann, H., Grundmann, J., 2020. Technical Note: Flow velocity and discharge measurement in rivers using terrestrial and unmanned-aerial-vehicle imagery. Hydrol. Earth Syst, Sci, p. 17.

Environment Canada, 2004. Procedures for conducting ADCP Discharge Measurements, 1st edition. ed. Environment Canada.

Escobar Villanueva, J.R., Iglesias Martínez, L., Pérez Montiel, J.I., 2019. DEM generation from fixed-wing UAV imaging and LiDAR-derived ground control points for flood estimations. Sensors (Basel) 19 (14), 3205.

Euler, L., 2008. Principles of the motion of fluids. Physica D: Nonlinear Phenomena, Euler Equations: 250 Years On 237, 1840–1854. https://doi.org/10.1016/j.physd.2008.04.019.

Fischer, J.L., Bennion, D., Roseman, E.F., Manny, B.A., 2015. Validation of a spatial model used to locate fish spawning reef construction sites in the St. Clair-Detroit River system. J. Great Lakes Res. 41, 1178–1184. https://doi.org/10.1016/j.jglr.2015.09.019.

Flener, C., Wang, Y., Laamanen, L., Kasvi, E., Vesakoski, J.-M., Alho, P., 2015. Empirical modeling of spatial 3D flow characteristics using a remote-controlled ADCP system: monitoring a spring flood. Water 7, 217–247. https://doi.org/10.3390/w7010217.

Fujita, I., Muste, M., Kruger, A., 1998. Large-scale particle image velocimetry for flow analysis in hydraulic engineering applications. J. Hydraul. Res. 36, 397–414. https://doi.org/10.1080/00221689809498626.

Fulton, J.W., Henneberg, M.F., Mills, T.J., Kohn, M.S., Epstein, B., Hittle, E.A., Damschen, W.C., Laveau, C.D., Lambrecht, J.M., Farmer, W.H., 2018. Computing under-ice discharge: a proof-of-concept using hydroacoustics and the Probability Concept. J. Hydrol. 562, 733–748. https://doi.org/10.1016/j.jhydrol.2018.04.073.

Fulton, J.W., Anderson, I.E., Chiu, C.-L., Sommer, W., Adams, J.D., Moramarco, T., Bjerklie, D.M., Fulford, J.M., Sloan, J.L., Best, H.R., Conaway, J.S., Kang, M.J., Kohn, M.S., Nicotra, M.J., Pulli, J.J., 2020a. QCam: sUAS-based doppler radar for measuring river discharge. Remote Sensing 12, 3317. https://doi.org/10.3390/rs12203317.

Fulton, J.W., Mason, C.A., Eggleston, J.R., Nicotra, M.J., Chiu, C.-L., Henneberg, M.F., Best, H.R., Cederberg, J.R., Holnbeck, S.R., Lotspeich, R.R., Laveau, C.D., Moramarco, T., Jones, M.E., Gourley, J.J., Wasielewski, D., 2020b. Near-field remote sensing of surface velocity and river discharge using radars and the probability concept at 10 U.S. geological survey streamgages. Remote Sens. 12, 1296. https://doi.org/10.3390/rs12081296.

Fulton, J., Ostrowski, J., 2008. Measuring real-time streamflow using emerging technologies: Radar, hydroacoustics, and the probability concept. J. Hydrol. 357, 1–10. https://doi.org/10.1016/j.jhydrol.2008.03.028.

Garcia, D., 2010. Robust smoothing of gridded data in one and higher dimensions with missing values. Comput. Stat. Data Anal. 54, 1167–1178. https://doi.org/10.1016/j.csda.2009.09.020.

M. Gard Flow-Habitat Relationships For Juvenile Spring/Fall-Run Chinook Salmon And Steelhead/Rainbow Trout Rearing In The Yuba River 2008.

Hankin, B., Metcalfe, P., Beven, K., Chappell, N.A., 2019. Integration of hillslope hydrology and 2D hydraulic modelling for natural flood management. Hydrol. Res. 50, 1535–1548. https://doi.org/10.2166/nh.2019.150.

Hauet, A., Morlot, T., Daubagnan, L., Paquier, A., Rivière, N., 2018. Velocity profile and depth-averaged to surface velocity in natural streams: a review over alarge sample of rivers. E3S Web Conf. 40, 06015.

Huang, H., 2018. Estimating uncertainty of streamflow measurements with moving-boat acoustic Doppler current profilers. Hydrol. Sci. J. 63, 353–368. https://doi.org/10.1080/02626667.2018.1433833.

Institute of Hydrology, 1999. Flood estimation handbook (five volumes). Centre for Ecology and Hydrology.

James, M.R., Chandler, J.H., Eltner, A., Fraser, C., Miller, P.E., Mills, J.P., Noble, T., Robson, S., Lane, S.N., 2019. Guidelines on the use of structure-from-motion photogrammetry in geomorphic research. Earth Surf. Proc. Land. 44, 2081–2084. https://doi.org/10.1002/esp.4637.

Javernick, L., Brasington, J., Caruso, B., 2014. Modeling the topography of shallow braided rivers using Structure-from-Motion photogrammetry. Geomorphology 213, 166–182. https://doi.org/10.1016/j.geomorph.2014.01.006.

Jodeau, M., Hauet, A., Coz, J.L., Bercovitz, Y., Lebert, F., 2017. LABORATORY AND FIELD LSPIV MEASUREMENTS OF FLOW VELOCITIES USING FUDAA-LSPIV, A FREE USER-FRIENDLY SOFTWARE 8.

Johnson, E.D., Cowen, E.A., 2017. Remote determination of the velocity index and mean streamwise velocity profiles. Water Resour. Res. 53, 7521–7535. https://doi.org/10.1002/2017WR020504.

Kasvi, E., Alho, P., Lotsari, E., Wang, Y., Kukko, A., Hyyppä, H., Hyyppä, J., 2015. Two-dimensional and three-dimensional computational models in hydrodynamic and

morphodynamic reconstructions of a river bend: sensitivity and functionality. Hydrol. Process. 29, 1604–1629. https://doi.org/10.1002/hyp.10277.
Kostaschuk, R., Best, J., Villard, P., Peakall, J., Franklin, M., 2005. Measuring flow velocity and sediment transport with an acoustic Doppler current profiler. Geomorphol. Fluid Flow Sedim. Trans. Process. Geomorphol. 68, 25–37. https://doi.org/10.1016/j.geomorph.2004.07.012.
Koutalakis, P., Tzoraki, O., Zaimes, G., 2019. UAVs for hydrologic scopes: application of a low-cost UAV to estimate surface water velocity by using three different image-based methods. Drones 3, 14. https://doi.org/10.3390/drones3010014.
Lane, S.N., Bradbrook, K.F., Richards, K.S., Biron, P.A., Roy, A.G., 1999. The application of computational fluid dynamics to natural river channels: three-dimensional versus two-dimensional approaches. Geomorphology 29, 1–20. https://doi.org/10.1016/S0169-555X(99)00003-3.
Le Coz, J., Hauet, A., Pierrefeu, G., Dramais, G., Camenen, B., 2010. Performance of image-based velocimetry (LSPIV) applied to flash-flood discharge measurements in Mediterranean rivers. J. Hydrol. 394, 42–52. https://doi.org/10.1016/j.jhydrol.2010.05.049.
Lee, J.-S., Julien, P.Y., 2006. Electromagnetic wave surface velocimetry. J. Hydraul. Eng. 132, 146–153. https://doi.org/10.1061/(ASCE)0733-9429(2006)132:2(146).
Legleiter, C.J., Kinzel, P.J., 2021. Surface flow velocities from space: particle image velocimetry of satellite video of a large, Sediment-Laden River. Front. Water 3, 652213. https://doi.org/10.3389/frwa.2021.652213.
Lewis, Q.W., Lindroth, E.M., Rhoads, B.L., 2018. Integrating unmanned aerial systems and LSPIV for rapid, cost-effective stream gauging. J. Hydrol. 560, 230–246. https://doi.org/10.1016/j.jhydrol.2018.03.008.
Liu, W.-C., Lu, C.-H., Huang, W.-C., 2021. Large-scale particle image velocimetry to measure streamflow from videos recorded from unmanned aerial vehicle and fixed imaging system. Remote Sensing 13, 2661. https://doi.org/10.3390/rs13142661.
Marini, G., De Martino, G., Fontana, N., Fiorentino, M., Singh, V.P., 2011. Entropy approach for 2D velocity distribution in open-channel flow. J. Hydraul. Res. 49, 784–790. https://doi.org/10.1080/00221686.2011.635889.
McCabe, M.F., Rodell, M., Alsdorf, D.E., Miralles, D.G., Uijlenhoet, R., Wagner, W., Lucieer, A., Houborg, R., Verhoest, N.E.C., Franz, T.E., Shi, J., Gao, H., Wood, E.F., 2017. The future of Earth observation in hydrology. Hydrol. Earth Syst. Sci. 21, 3879–3914. https://doi.org/10.5194/hess-21-3879-2017.
Moramarco, T., Barbetta, S., Tarpanelli, A., 2017. From surface flow velocity measurements to discharge assessment by the entropy theory. Water 9, 120. https://doi.org/10.3390/w9020120.
Moriasi, D.N., Arnold, J.G., Van Liew, M.W., Bingner, R.L., Harmel, R.D., Veith, T.L., 2007. Model evaluation guidelines for systematic quantification of accuracy in watershed simulations. Trans. ASABE 50, 885–900. https://doi.org/10.13031/2013.23153.
Mueller, D.S., Wagner, C.R., Rehmel, M.S., Oberg, K.A., Rainville, F., 2013. Measuring discharge with acoustic Doppler current profilers from a moving boat (USGS Numbered Series No. 3-A22), Measuring discharge with acoustic Doppler current profilers from a moving boat, Techniques and Methods. U.S. Geological Survey, Reston, VA. https://doi.org/10.3133/tm3A22.
Muste, M., Fujita, I., Hauet, A., 2008. Large-scale particle image velocimetry for measurements in riverine environments. Water Resour. Res. 44 https://doi.org/10.1029/2008WR006950.
Naves, J., García, J.T., Puertas, J., Anta, J., 2021. Assessing different imaging velocimetry techniques to measure shallow runoff velocities during rain events using an urban drainage physical model. Hydrol. Earth Syst. Sci. 25, 885–900. https://doi.org/10.5194/hess-25-885-2021.
Parsapour-Moghaddam, P., Rennie, C.D., 2018. Calibration of a 3D hydrodynamic meandering river model using fully spatially distributed 3D ADCP velocity data. J. Hydraul. Eng. 144, 04018010. https://doi.org/10.1061/(ASCE)HY.1943-7900.0001424.
Pasternack, G.B., Gilbert, A.T., Wheaton, J.M., Buckland, E.M., 2006. Error propagation for velocity and shear stress prediction using 2D models for environmental management. J. Hydrol. Measurem. Parameteriz. Rainfall Microstruct. 328, 227–241. https://doi.org/10.1016/j.jhydrol.2005.12.003.
Pasternack, G.B., 2011. 2D Modeling and Ecohydraulic Analysis.
Patalano, A., García, C.M., Rodríguez, A., 2017. Rectification of image velocity results (RIVeR): a simple and user-friendly toolbox for large scale water surface Particle Image Velocimetry (PIV) and Particle Tracking Velocimetry (PTV). Comput. Geosci. 109, 323–330. https://doi.org/10.1016/j.cageo.2017.07.009.
Pearce, S., Ljubičić, R., Peña-Haro, S., Perks, M., Tauro, F., Pizarro, A., Dal Sasso, S., Strelnikova, D., Grimaldi, S., Maddock, I., Paulus, G., Plavšić, J., Prodanović, D., Manfreda, S., 2020. An Evaluation of image velocimetry techniques under low flow conditions and high seeding densities using unmanned aerial systems. Remote Sens. 12, 232. https://doi.org/10.3390/rs12020232.
Perks, M.T., Sasso, S.F.D., Hauet, A., Jamieson, E., Coz, J.L., Pearce, S., Peña-Haro, S., Pizarro, A., Strelnikova, D., Tauro, F., Bomhof, J., Grimaldi, S., Goulet, A., Hortobágyi, B., Jodeau, M., Käfer, S., Ljubicic, R., Maddock, I., Mayr, P., Paulus, G., Pénard, L., Sinclair, L., Manfreda, S., 2020. Towards harmonisation of image velocimetry techniques for river surface velocity observations 15.
Pilotti, M., Milanesi, L., Bacchi, V., Tomirotti, M., Maranzoni, A., 2020. Dam-break wave propagation in alpine valley with HEC-RAS 2D: experimental cancano test case. J. Hydraul. Eng. 146, 05020003. https://doi.org/10.1061/(ASCE)HY.1943-7900.0001779.
Pizarro, A., Dal Sasso, S.F., Perks, M.T., Manfreda, S., 2020a. Identifying the optimal spatial distribution of tracers for optical sensing of stream surface flow. Hydrol. Earth Syst. Sci. 24, 5173–5185. https://doi.org/10.5194/hess-24-5173-2020.
Pizarro, A., Sasso, S.F.D., Perks, M.T., Manfreda, S., 2020b. Identifying the optimal spatial distribution of tracers for optical sensing of stream surface flow. Hydrol. Earth Syst. Sci. 13.
Pumo, D., Alongi, F., Ciraolo, G., Noto, L.V., 2021. Optical Methods for river monitoring: a simulation-based approach to explore optimal experimental setup for LSPIV. Water 13, 247. https://doi.org/10.3390/w13030247.
R Core Team Rf. R: A language and environment for statistical computing 2013 R foundation for statistical computing Vienna Austria.
Ran, Q., Li, W., Liao, Q., Tang, H., Wang, M., 2016. Application of an automated LSPIV system in a mountainous stream for continuous flood flow measurements. Hydrol. Process. 30, 3014–3029. https://doi.org/10.1002/hyp.10836.
Refsgaard, J.C., Henriksen, H.J., 2004. Modelling guidelines—terminology and guiding principles. Adv. Water Resour. 27, 71–82. https://doi.org/10.1016/j.advwatres.2003.08.006.
Rennie, C.D., Church, M., 2010. Mapping spatial distributions and uncertainty of water and sediment flux in a large gravel bed river reach using an acoustic Doppler current profiler. J. Geophys. Res. Earth Surf. 115 https://doi.org/10.1029/2009JF001556.
Sawyer, A.M., Pasternack, G.B., Moir, H.J., Fulton, A.A., 2010. Riffle-pool maintenance and flow convergence routing observed on a large gravel-bed river. Geomorphology 114, 143–160. https://doi.org/10.1016/j.geomorph.2009.06.021.
M. Schumann Andreadis, Rapid Mapping of Small-Scale River-Floodplain Environments Using UAV SfM Supports Classical Theory Remote Sensing 11 2019 982 10.3390/rs11080982.
Shannon, C.E., 1948. A mathematical theory of communication. Bell Syst. Tech. J. 27, 379–423. https://doi.org/10.1002/j.1538-7305.1948.tb01338.x.
Shustikova, I., Domeneghetti, A., Neal, J.C., Bates, P., Castellarin, A., 2019. Comparing 2D capabilities of HEC-RAS and LISFLOOD-FP on complex topography. Hydrol. Sci. J. 64, 1769–1782. https://doi.org/10.1080/02626667.2019.1671982.
Simpson, M.R., 2001. Discharge measurements using a broad-band acoustic Doppler current profiler. US Department of the Interior, US Geological Survey Reston.
Smith, M.W., Carrivick, J.L., Hooke, J., Kirkby, M.J., 2014. Reconstructing flash flood magnitudes using 'Structure-from-Motion': a rapid assessment tool. J. Hydrol. 519, 1914–1927. https://doi.org/10.1016/j.jhydrol.2014.09.078.
Stott, E., Williams, R.D., Hoey, T.B., 2020. Ground Control point distribution for accurate kilometre-scale topographic mapping using an RTK-GNSS unmanned aerial vehicle and SfM photogrammetry. Drones 4, 55. https://doi.org/10.3390/drones4030055.
Tauro, F., Piscopia, R., Grimaldi, S., 2017. Streamflow Observations from cameras: large-scale particle Image velocimetry or particle tracking velocimetry?: STREAMFLOW FROM CAMERAS: LSPIV OR PTV? Water Resour. Res. 53, 10374–10394. https://doi.org/10.1002/2017WR020848.
Thielicke, W., Stamhuis, E., 2014. PIVlab – Towards user-friendly, affordable and accurate digital particle image velocimetry in MATLAB. J. Open Res. Softw. 2, e30.
Tiffan, K.F., Garland, R.D., Rondorf, D.W., 2002. Quantifying flow-dependent changes in subyearling fall chinook salmon rearing habitat using two-dimensional spatially explicit modeling. North Am. J. Fish. Manage. 22 (3), 713–726.
Tokarczyk, P., Leitao, J.P., Rieckermann, J., Schindler, K., Blumensaat, F., 2015. High-quality observation of surface imperviousness for urban runoff modelling using UAV imagery. Hydrol. Earth Syst. Sci. 19, 4215–4228. https://doi.org/10.5194/hess-19-4215-2015.
Wagner, C.R., Mueller, D.S., 2001. Calibration and Validation of a Two-dimensional Hydrodynamic Model of the Ohio River, Jefferson County, Kentucky. U.S. Department of the Interior, U.S. Geological Survey.
Welber, M., Le Coz, J., Laronne, J.B., Zolezzi, G., Zamler, D., Dramais, G., Hauet, A., Salvaro, M., 2016. Field assessment of noncontact stream gauging using portable surface velocity radars (SVR): FIELD ASSESSMENT OF PORTABLE SURFACE VELOCITY RADARS. Water Resour. Res. 52, 1108–1126. https://doi.org/10.1002/2015WR017906.
Wilcock, P.R., 1996. Estimating local bed shear stress from velocity observations. Water Resour. Res. 32, 3361–3366. https://doi.org/10.1029/96WR02277.
Wildhaweswater, Site Manager's Journal: Restoring Swindale Beck. Wild Haweswater 2020 accessed 1.24.21.
Williams, R.D., Brasington, J., Hicks, M., Measures, R., Rennie, C.D., Vericat, D., 2013. Hydraulic validation of two-dimensional simulations of braided river flow with spatially continuous aDcp data. Water Resour. Res. 49, 5183–5205. https://doi.org/10.1002/wrcr.20391.
Williams, R.D., Rennie, C.D., Brasington, J., Hicks, D.M., Vericat, D., 2015. Linking the spatial distribution of bed load transport to morphological change during high-flow events in a shallow braided river: Spatially distributed bedload transport. J. Geophys. Res. Earth Surf. 120, 604–622. https://doi.org/10.1002/2014JF003346.
Wing, O.E.J., Bates, P.D., Sampson, C.C., Smith, A.M., Johnson, K.A., Erickson, T.A., 2017. Validation of a 30 m resolution flood hazard model of the conterminous United States: 30 m Resolution Flood Model Of Conus. Water Resour. Res. 53, 7968–7986. https://doi.org/10.1002/2017WR020917.
Yalcin, E., 2020. Assessing the impact of topography and land cover data resolutions on two-dimensional HEC-RAS hydrodynamic model simulations for urban flood hazard analysis. Nat Hazards 101, 995–1017. https://doi.org/10.1007/s11069-020-03906-z.